3D printing of micro/nano-hierarchical structures with various structural stiffness for controlling friction and deformation

Mahyar Afshar-Mohajer[1,2], Xingwei Yang[3], Rong Long[3], and Min Zou[1,2*]

[1]Department of Mechanical Engineering, University of Arkansas, Fayetteville, AR 72701, USA

[2]Center for Advanced Surface Engineering, University of Arkansas, Fayetteville, AR 72701, USA

[3]Department of Mechanical Engineering, University of Colorado Boulder, Boulder, CO 80309, USA

* To whom correspondence should be addressed. Tel.: (479) 575-6671, Fax: (479) 575-6982, E-mail: mzou@uark.edu.

Abstract

Micro/nano-hierarchical structures are the building blocks of textured functional surfaces. Having control over the 3D shapes of these building blocks will lead to better control over their friction and deformation when in contact with other surfaces, paving the way for better-engineered surfaces. In this study, a high-resolution two-photon lithography additive manufacturing technique was utilized to produce micro/nano-hierarchical structures composed of nanohairs on top of micropillars. Varying the tapering angle of the micropillar and the length of the nanohairs enabled control over the effective stiffness of the micro/nano-hierarchical structures. Individual micro/nano-hierarchical structures were subjected to normal and tangential loading inside a scanning electron microscope, which enabled in-situ monitoring of the structural deformation in addition to their frictional response. This study revealed that changes in the structure stiffness by varying the tapering angle resulted in changes in the onset of sliding motion, friction force, and coupling between the deformation of the nanohair and the micropillar, thereby providing a new direction for friction and deformation control by tailoring structure stiffness through 3D printing.

Keywords: Two-photon lithography; Structural stiffness; In-situ SEM tribology; Buckling; Hydrophobicity

1. Introduction

The ability to engineer interactions between surfaces has been gaining increasing importance. This is because such capability has enabled the development of surfaces with a wide variety of tailored functionalities, such as friction reduction [1–3] or enhancement [4–7], surface wettability manipulation [8–11], structural color generation [12,13], and even cell culture manipulation [14–16]. One of the main routes to achieving and manipulating surface functionalities is to introduce micro/nano-hierarchical structures to surfaces. This has been inspired by nature [17], whereby depending on the surface functionality, the micro and nano structures play distinct roles in achieving that functionality [18].

Examples of such natural surfaces are found in adhesive gecko feet that have microscale structures known as seta that branch off into nanoscale projections known as spatulae [19], butterfly wings with structural color and directional adhesion that consist of micro-ribs with nanoridges [20], rose petals with high water adhesion which are made up of micropapillae covered with nanofolds [21], and superhydrophobic lotus leaves that have micro/nano-hierarchical textures made up of micropapillae covered with nanohairs [22].

The development of superhydrophobic surfaces inspired by lotus leaves, in particular, has attracted much attention due to their potential for self-cleaning [23], open microfluidics [24], oil/water separation [25], and buoyancy applications [26]. Since micro/nano-structures, such as lotus leaf-like surfaces, can reduce the real area of contact between surfaces and thus reduce the friction between them, they have also been studied for friction reduction [27]. Therefore, it is important to have control over the frictional responses of micro/nano-textured surfaces to enable new applications. For example, microelectromechanical systems (MEMS) suffer from high

adhesion and friction between rubbing surfaces [28–30]. Having lotus leaf-like superhydrophobic surfaces not only could reduce meniscus-mediated adhesion but also enable sliding motion by reducing friction.

Even when the primary functionalities of the micro/nano-hierarchies are not concerned with their friction, surface topography directly determines its deformation properties under shear force, which affects the texture durability. For example, the high aspect ratio structures needed for superhydrophobicity are susceptible to structural deformation, which has been a hurdle that prevents their widespread application [31,32]. More control over frictional interactions between textured interfaces can provide solutions to some of the inherent limitations of textures.

Small-scale structures such as microstructures, nanostructures, and micro/nano-hierarchical structures are the building blocks of textured surfaces. Having control over their precise fabrication and testing will enable a better understanding of their mechanical behavior. This will lead to better-engineered textured surfaces that will not only overcome their inherent limitations but also allow the conception of novel surfaces, components, and applications.

So far, only a limited number of studies have explored the potential of 3D modifications of surface micro/nano-structures [33–35]. The advancements in small-scale 3D printing methods with micro/nano-scale resolution [36–38], such as two-photon lithography (TPL) [39], laser-induced forward transfer [40], and electrohydrodynamic inkjet printing [41], enabled new opportunities to study and engineer micro/nano-hierarchical structures for controlling friction.

In this study, the frictional and deformation behavior of 3D micro/nano-hierarchical structures inspired by lotus leaves were systematically studied to understand how they are affected by the texture structural stiffness. Lotus leaf-inspired structures were chosen due to their

hydrophobicity which can reduce adhesion force in MEMS applications in addition to reducing friction in sliding contact. TPL was selected to fabricate the structures due to its simplicity and versatility. Micropillars with three different base dimensions (small-base, medium-base, and large-base) covered with nanohairs of different lengths (no-hair, short-hair, and long-hair) were fabricated, resulting in a combination of nine structures with different structural stiffness.

A major challenge in understanding how 3D shapes of the structures affect their deformation when subject to normal and tangential loading has been the lack of in-situ observation. In this study, we subjected individual micro/nano-hierarchical structures to normal and tangential loading inside a scanning electron microscope (SEM), which enabled in-situ monitoring of the structural deformation in addition to their frictional force response. This resulted in not only discoveries in the relationships between the stiffness of the structures and their frictional force and deformation response but also new insights into the effects of modifying the 3D shapes of the structures on the onset of relative motion.

2. Materials and methods

2.1 Sample fabrication

A two-photon lithography (TPL) machine that is commercially available (Photonic Professional GT, Nanoscribe GmbH) was used for additive manufacturing of the micro/nano-structures. In TPL, tight focusing of the laser into a very small volume within the photoresist enables curing of the volume (known as voxel) due to two-photon absorption [39], resulting in the high resolution of this technique. For the structures in this study, CAD models of micropillars with three different base dimensions were imported into the software Describe (Nanoscribe GmbH) for slicing. The micropillars were printed using the ‘continuous mode’ as shown in Fig. 1a.i, whereby

the voxel was scanned continuously along the printing path within the same layer using the galvo scanning mirrors, curing the IP-DIP photoresist (Nanoscribe GmbH). To print the next layer, the piezo stage moved in the direction of the height of the structure at a slicing distance of 1 μm. To form the nanohairs, individual voxels were placed on top of the printed micropillars as shown in Fig. 1a.ii. Different lengths of nanohair were achieved by programming the individual voxels to be placed at different "z-offset" values relative to the top layer of the micropillar. Fig. 1b shows the combination of three micropillar base dimensions and three nanohair lengths resulting in 9 unique structure types with the exact dimensions described in Section 3.1.

To accelerate the sample fabrication process, replication of the 3D printed structures was carried out using soft lithography. To make the mold for soft lithography, parts A and B of SYLGARD 184 polydimethylsiloxane (PDMS, Dow Inc.) were mixed (10:1 ratio) and poured on the 3D-printed master and cured overnight at 55 °C in an oven. After curing, the mold was separated from the master. To replicate the samples, the PDMS mold and a glass substrate were used to sandwich the IP-DIP photoresist using a 1 kg mass under UV light (BlueWave 200, Dymax Corp.) for 800 s (600 s through the PDMS mold and then 200 s after removal of the mold) at a power density of 300 mW/cm^2.

The printed masters and replicated surfaces were silanized using vaporized Perfluorodecyltrichlorosilane (FDTS, Sigma-Aldrich Co.). This was done to facilitate detachment of the cured PDMS mold from the printed masters by preventing the structures from adhering to the mold and making the replicated surfaces hydrophobic. Before silanizing the surfaces by placing them together with FDTS droplets inside a vacuum chamber, surfaces were treated with oxygen plasma (PE25, Plasma Etch Inc.) for a duration of 20 s at a power of 150 W and a pressure of 200 mTorr.

2.2 Tribological testing of micro/nano-hierarchical structures inside an SEM

The samples containing the micro/nano-hierarchical structures were mounted on a Picoindenter (PI-88, Bruker) that has both lateral and normal force sensors. The Picoindenter was then placed inside a VEGA3 SEM (TESCAN OSRAY HOLDING, a.s.) and the tribological testing was carried out on individual micro/nano-structures. Fig. 1c shows a schematic view of the testing. A flat-ended conical tip (10 μm diameter at the flat end) was used as the counterface to subject a structure to an applied normal load (downward arrow) and relative lateral movement (leftward and rightward arrows). The structures were subjected to one cycle of tribological testing that included a 5 μm forward stroke and a 5 μm backward stroke at a speed of 1 μm/s. It should be noted that the lateral motion was provided by the piezo stage on which the samples were mounted. The horizontal arrows shown in Fig. 1 and the rest of the paper represent the relative motion of the probe to the sample. Fig. 1d illustrates examples of the in-situ SEM views of the structures while being tested and showcases the direct monitoring of deformation in the structures as they were subjected to normal and tangential loading. Humidity was negligible as the tests were conducted inside a high vacuum SEM chamber. Five repeat tests were conducted on five unique structures of each hierarchy type. Results are presented as mean ± standard error.

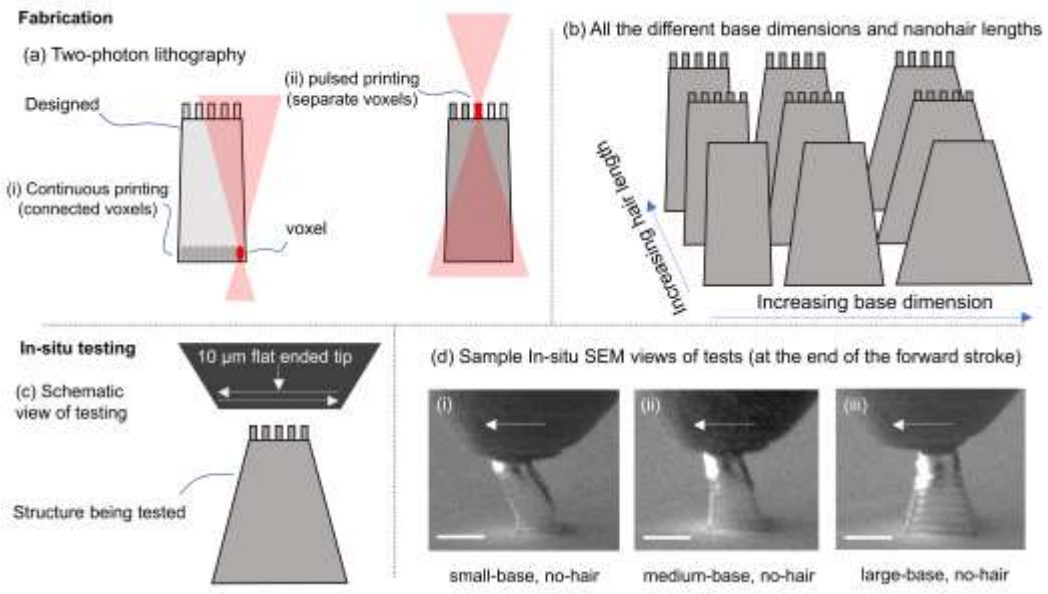

Fig. 1. Fabrication and testing of micro/nano-hierarchical structures: (a) two-photon lithography of micro/nano-hierarchical structures, (b) different structure types as a result of the combination of different micropillar base dimensions (small-base, medium-base, large-base) and nanohair lengths (long-hair, short-hair, no-hair), (c) schematic view of in-situ SEM testing of a structure subjected to normal and tangential loading, and (d) examples of SEM views of the structures being tested showcasing the ability of the method to observe the deformation of structures (scale bars: 5 μm).

2.3 Water contact angle (WCA) measurement

The WCAs of the textured surfaces were measured using an OCA 15 contact angle goniometer (DataPhysics Instruments GmbH, Germany). Water droplets of 9 μL in volume were deposited on the textured surfaces for the measurement of the static WCAs. This large droplet volume was chosen since smaller droplets could not be placed on textured surfaces with long-hair structures because of their superhydrophobicity. To calculate the contact angle hysteresis, advancing and receding WCAs were recorded by measuring the WCA while increasing (advancing) and decreasing (receding) the volume of the water droplet deposited on the surface.

WCA was measured on three samples, and the measurements were repeated three times on each sample. Results are presented as mean ± standard error.

2.4 Microscopy and imaging

VK-X260K 3D laser scanning confocal microscope (Keyence Corp.) was utilized for measuring the fabricated structures. VEGA3 SEM (TESCAN OSRAY HOLDING, a.s.) was used for the imaging of the textured surfaces and the in-situ observation of the structures during tribological testing inside the SEM.

2.5 Finite element analysis

Micro/nano-hierarchical structures subjected to tribological testing were analyzed by finite element analysis (FEA) using the ABAQUS software package (version 2020, Simulia, Providence, RI, USA) following the same procedures described in previous work [42]. Briefly, the FEA model consists of a rigid block representing the probe and a deformable hierarchical structure below the rigid block. The underlying material of the deformable hierarchical structure, i.e., IP-DIP photoresist, was treated as an elastic-plastic solid, which was motivated by the tensile testing data of the IP-DIP photoresist reported in the literature [43]. Specifically, the elastic component was modeled as a neo-Hookean solid with Young's modulus of 2.6 GPa and Poisson's ratio of 0.49, while the plastic component was modeled using a linear isotropic hardening behavior with the yield stress, hardening modulus, and ultimate strength of 80 MPa, 300 MPa, and 600 MPa, respectively [42]. Coulomb friction model was used to simulate the contact interface with a friction coefficient of 0.4 which was obtained by calibrating the model based on the results of the experimental tribological tests. 3D models were constructed for the no-hair micro-pillars. However, for the micro-pillar with short-hairs and long-hairs, 3D simulations were challenging

since the ten-fold difference in the size of the micro-pillar and nanohair requires drastically increased computational cost and is difficult to converge. Therefore, for the nanohairs + micropillar structures, two-dimensional (2D) plane strain models were adopted. The dimensions of the 3D no-hair micro-pillars were set to be the experimentally measured values as shown in Fig. 2b. In the 2D models for nanohairs + micropillar structures, the geometry of the micro-pillar was simplified to a trapezoid. The nanohairs were added as five evenly spaced rectangles on the top edge of the micro-pillar. A detailed description of FEA simulations (e.g., mesh, material model, and analysis steps) can be found in Afshar-Mohajer et al. [42].

3. Results and discussions

3.1 Imaging and structure dimensions

The combination of three micropillar base dimensions (small-base, medium-base, and large-base), and three nanohair lengths (no-hair, short-hair, and long-hair), produced 9 distinct structures. Fig. 2a shows SEM images of structures in a matrix, where moving horizontally (left to right) and vertically (top to bottom) in the matrix represents increasing the base dimension of the micropillar and decreasing the nanohair length, respectively. Micro/nano-hierarchical structures have reduced effective stiffness compared to micropillar (no-hair) structures [44,45]. Therefore, the principal diagonal of the matrix (from top left to bottom right) represents moving from the structure with the lowest to the highest structural stiffness. Detailed dimensions of the structures are provided in Fig. 2b by stacking the dimensions of all structures in one compact figure. This schematic drawing of the structures shows the variable dimensions, namely micropillar base and nanohair height by dotted arrows, and the constant dimensions, i.e., the micropillar height, the diameter of the

nanohairs, and the center-to-center distance between individual nanohairs are presented by solid arrows.

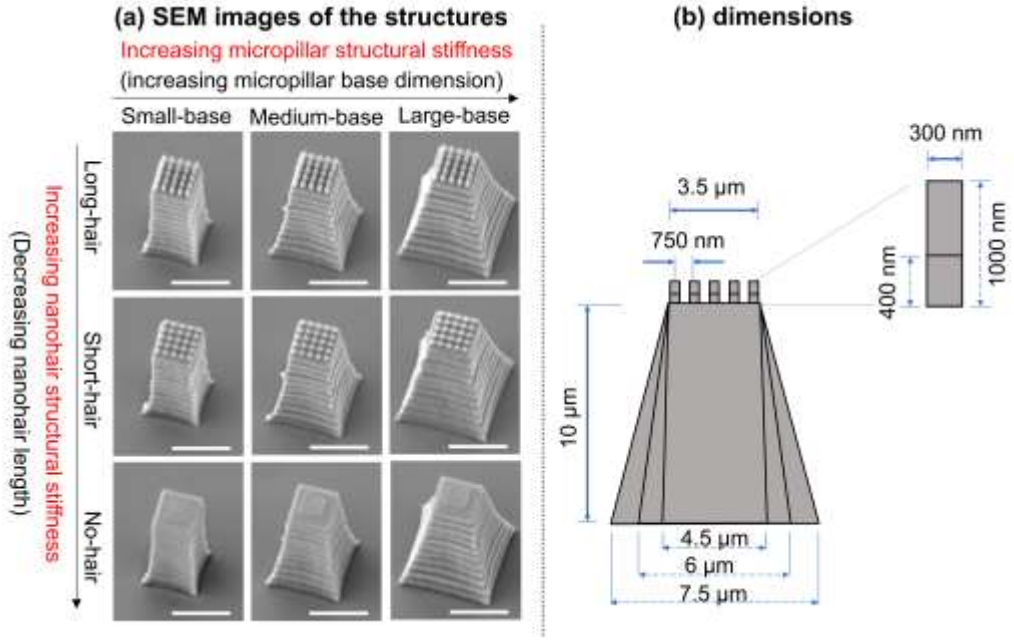

Fig. 2. The geometries and dimensions of the printed structures. (a) SEM images of the structures. The structures in each row have the same hair length and those in each column have the same base dimensions (Scale bars: 5 μm). (b) A unified schematic of all the structures showing their dimensions for comparison with each other.

3.2 Effect of base dimension on the static friction and the onset of relative motion of no-hair structures

To discuss the impact of the shape of structures on static friction, no-hair structures (micropillar only) are examined first. Fig. 3 shows the representative plots of lateral force versus lateral displacement of one-cycle (i.e., a forward lateral displacement followed by a backward lateral displacement) tribological tests together with their corresponding in-situ SEM snapshots at

points specified on the force profiles under the smallest (400 μN in Figs. 3a and 3b) and the largest applied normal loads (1000 μN in Figs. 3c and 3d).

3.2.1 Forward stroke (from point 1 to point 3)

Fig. 3a shows that the slopes of the lateral force profiles between points 1 and 2 (the static friction region before the occurrence of relative sliding between the counterface and the structure) are steeper for larger base structures. This means that the onset of relative motion between the sliding surfaces occurred sooner for structures with a larger base. The corresponding SEM snapshots of the in-situ tests subjected to a normal load of 400 μN are presented in Fig. 3b. The small-base structure showed observable bending in the sliding direction at point 2. The lower flexural stiffness due to the smaller base dimension resulted in more bending of the micropillar before the relative sliding of the counterface started and delayed the onset of relative motion.

When a larger normal load was applied (Figs. 3c and 3d), the bending of the structures became more noticeable as shown in the snapshots accompanying the lateral force plots for the case with 1000 μN applied normal load (Fig. 3d). The slopes during the static friction region still maintained their order (Fig. 3c): steeper slopes for larger base dimensions. It can be seen, however, that the lateral force plot of the small-base structure does not contain a steady-state plateau. The corresponding SEM snapshots of the small-base micropillar not only show the structure underwent the largest bending but the least relative motion during the forward stroke. The counterface and micropillar were constantly in contact without any sliding (Video S1, Supplementary Material). Point 2 is the peak force, after which the small-base micropillar started undergoing substantial bending, resulting in the negative lateral force slope until point 3 at the end of the forward stroke.

3.2.2 Backward stroke (from point 3 to point 5)

When the forward stroke ends, the backward stroke is started by moving the counterface laterally in the opposite direction, as indicated by points 3 through 5. The same relationship between the base dimension and the pre-sliding slope can also be observed during the return motion between points 3 and 4. Similar to the forward stroke, the small-base structure under the 1000 μN normal load did not exhibit a steady-state friction region as the backward stroke was completely expended by the recovery of the bent structure, and hence there was no relative movement between the structure and the counterface, as shown by the SEM snapshots (Fig. 3d), and Video S1 in the Supplementary Material.

It can be further noted that the lateral displacement to overcome static friction during the backward stroke (the region between points 3 and 4) is larger than the static friction region during the forward stroke (the region between points 1 and 2). This is because, during the forward stroke, the micropillar underwent bending from an initially straight profile, while during the backward stroke, recovery of the already bent structure implies that a larger backward lateral displacement is needed to achieve the same level of backward lateral force. This also resulted in a shorter actual sliding distance during the backward stroke (compare the lateral displacement between points 4 and 5 to the lateral displacement between points 2 and 3).

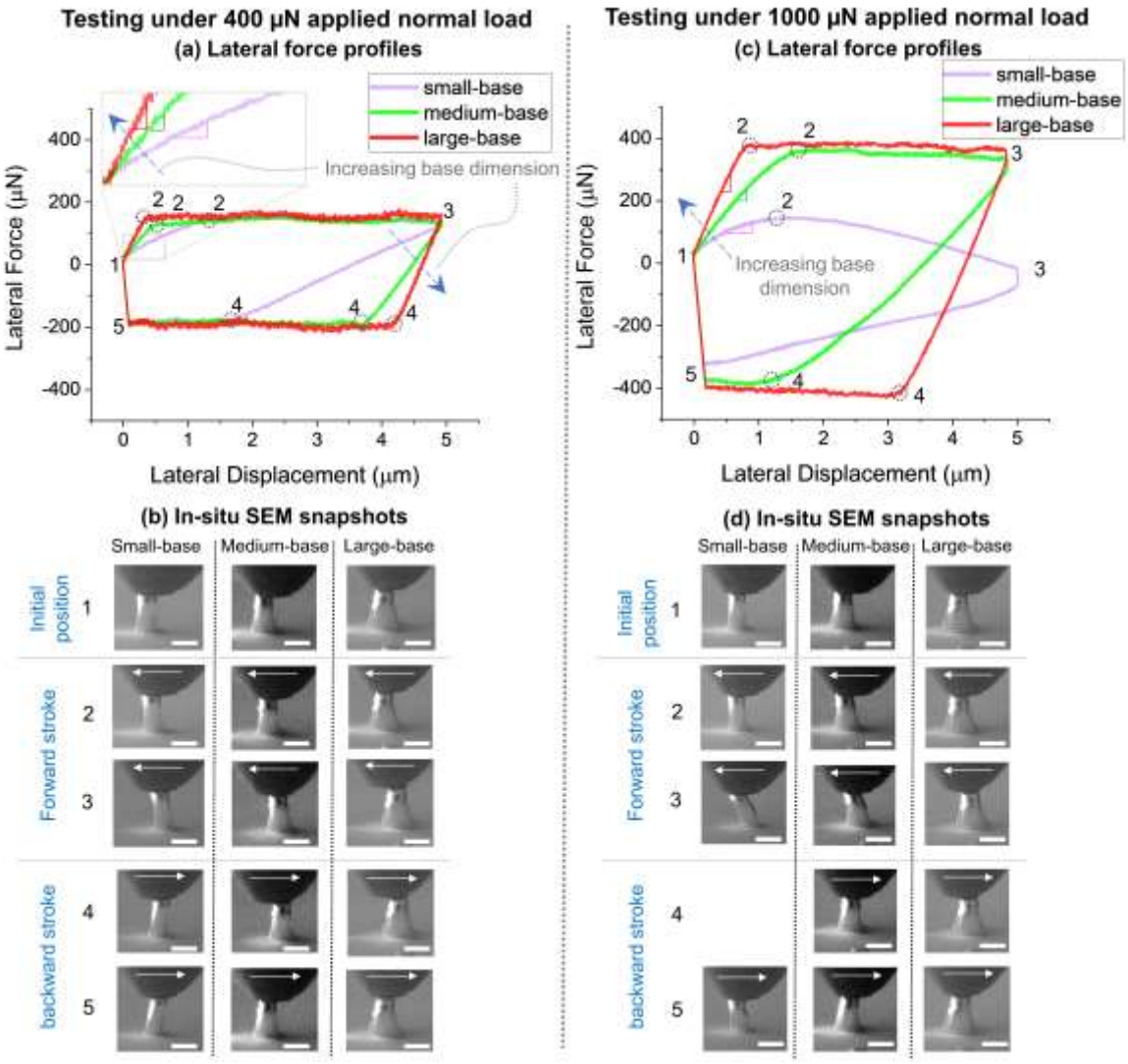

Fig. 3. Lateral force profiles and in-situ SEM snapshots of no-hair (micropillar only) structures under (a-b) 400 μN applied normal load, and (c-d) 1000 μN applied normal load (white arrows in the in-situ SEM images indicate the direction of the relative movement of the counterface. Scale bars: 5 μm)

3.3 Effect of the applied normal load on the lateral force response of no-hair structures

To further study the impact of the applied normal load, Figs. 4a-c shows the lateral force profiles of the no-hair structures at four different applied normal loads (400, 600, 800, and 1000 μN). The in-situ SEM snapshots (Figs. 4d-f) show the maximum structure deformation at the end of the forward stroke (marked with a filled circle on the lateral force profile). The small-base micropillar showed no steady-state horizontal region at applied normal loads above 400 μN (Fig. 4a). Instead, the data consisted of a peak force followed by negative slopes. This is very similar to the phenomenon observed in our previous studies [42,46], which is attributed to the severe bending of small-scale structures happening before any interfacial sliding could occur. Bending became more prominent at larger normal loads, as indicated by the downward dashed arrow (Fig. 4a) and the in-situ SEM snapshots (Fig. 4d), as increasing the normal load increased the threshold lateral force for sliding (i.e., the static friction).

Comparing the lateral force loops of the small-base structures (Fig. 4a) to those of medium-base and large-base structures (Figs. 4b and 4c), it is evident that, as the base dimension increased, a steady-state kinetic friction region due to the relative sliding of the contacting surfaces was observed, as opposed to the constant sticking during the small-base tests at loads above 400 μN. The medium-base and large-base structures, which did not show the extreme deformation of the small-base structures with the increasing applied normal load (Figs. 4e and 4f), exhibited the expected friction increase with the increasing normal load.

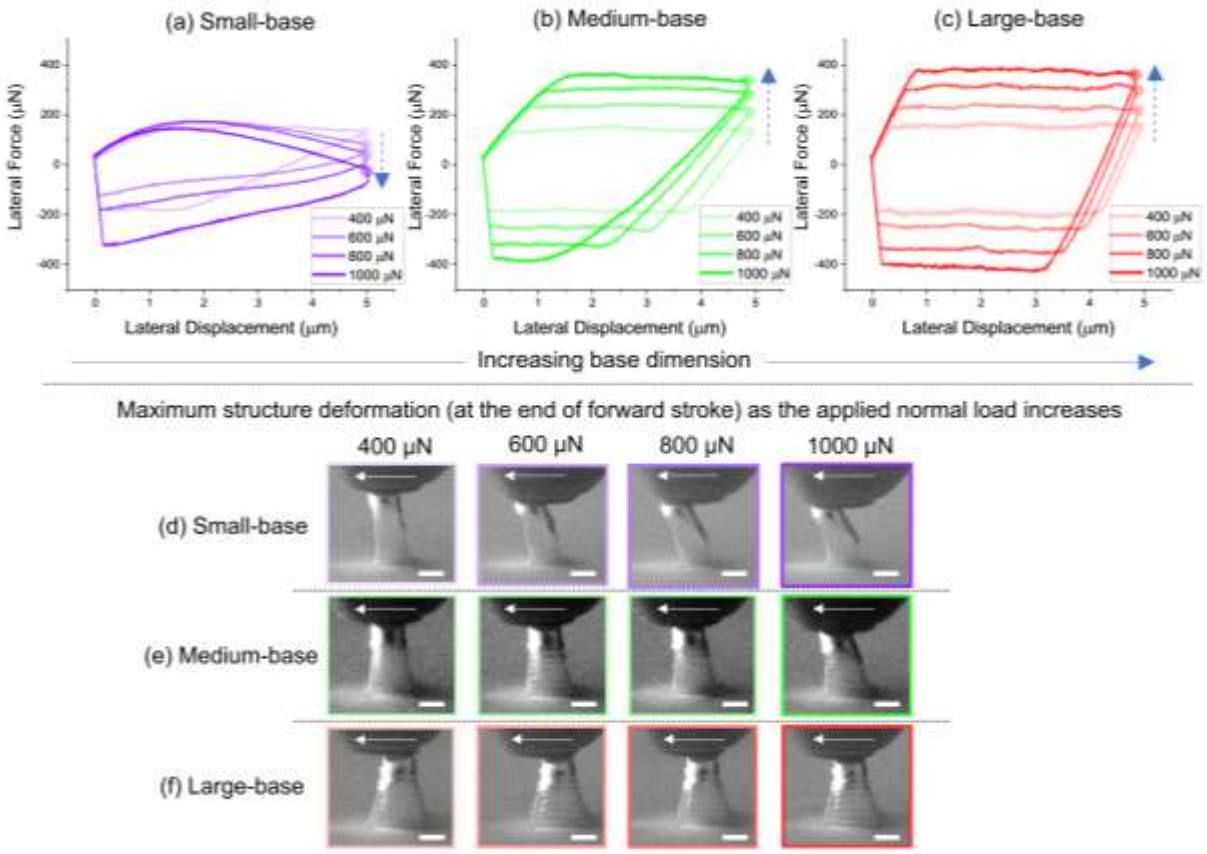

Fig. 4. Effect of increasing the applied normal load on the lateral forces of (a) small-base, (b) medium-base, and (c) large-base structures. In-situ SEM snapshots of (d) small-base, (e) medium-base, and (f) large-base structures as the forward stroke came to an end (Scale bars: 3 μm).

3.4 Lateral force profile of micro/nano-hierarchical structures (short-hair and long-hair structures)

Fig. 5 shows the lateral force loops of the hierarchical structures, i.e. short-hair (Figs. 5a and 5b) and long-hair structures (Figs. 5c and 5d) subjected to the normal loads of 400 μN and 1000 μN. The incipient sliding regions of the lateral force profiles of the short-hair structures under 400 μN (Fig. 5a) and 1000 μN (Fig. 5b) normal loads showed the same trend as observed in no-hair structures: increasing slope with increasing base dimension. However, there are obvious oscillations/undulations in the lateral force profiles of the short-hair structures (Figs. 5a and 5b),

which were not observed in those of the no-hair and long-hair structures. These oscillations of friction force from textured surfaces have been observed when using a counterface that is smaller than the spacing between the texture features [47] or when the counterface covers multiple features [48]. The observed pattern is quasiperiodic, meaning that there are variations between and within the tests [49]. Interestingly, Fig. 5b shows that the distance between the two force peaks for the large-base structure is around 1μm, which is very close to the distance between the centers of two short nanohairs (~750 nm) plus the diameter of the nanohair (~300 nm). Fig. 5c shows a magnified view of the lateral force profile of the short-hair + large-base structure during the forward stroke of the test, along with the normal displacement of the counterface. Note that the smoothed data using a 100-point adjacent averaging is shown together with the raw data in Fig. 5c. The underlying physical mechanism of the force oscillations may be attributed to repeated stick-slip cycles of the short nanohairs, i.e., the nanohairs first underwent bending while remaining adhered to the counterface and then slide back suddenly under sufficiently large lateral force. Fig. 5c supports this explanation by showing that the lateral force oscillations are in sync with the normal displacement oscillations. In other words, when the normal displacement increased (positive slope) due to the bending of short nanohairs, the lateral force also increased (positive slope) due to sticking. When the normal displacement decreased (negative slope), the lateral force also reduced due to slip. This can explain why such oscillations were absent in the no-hair or long-hair structures since the former lacked a well-defined pattern and the latter underwent buckling and collapse of nanohairs, both of which resulted in sliding of the counterface on a more flattened surface in comparison to the short-hair structures.

The addition of long nanohairs (Figs. 5d and 5e) resulted in more significant changes in the behavior of the structures, specifically in the incipient sliding region (between points 1 and 2).

Firstly, as seen in Fig. 5d, the lateral force exhibits a unique behavior between points 1 and 2 whereby instead of transitioning to a steady-state sliding regime with a fixed slope, there is an initial positive slope (between points 1 and 1.1), followed by a negative slope (between points 1.1 and 1.2) and a final positive slope (between points 1.2 and 2) that transitioned to steady-state sliding. This indicates a multi-step incipient sliding due to the hierarchy of the structure as discussed in our previous papers [42,46]. Upon initial contact, the nanohairs resist sliding, resulting in an increase in friction and a positive slope. Further lateral movement of the stage causes the nanohair to bend, resulting in a negative slope. Interestingly, the lateral force pattern observed between points 1 and 1.2 of the long-hair structure (Fig. 5d) is similar to the pattern seen when small-base structures of any hair length are subjected to the largest normal load (Fig. 3c, Fig. 5b, and Fig. 5e) as they also underwent bending due to their lower stiffness, except for the fact that bending of long nanohairs happened under smaller applied normal loads comparing to small-base micropillars. When subjecting the long-hair structures to 1000-μN applied normal load, the lateral force profiles (Fig. 5e) did not exhibit the same signature as in Fig. 5d. This is because the higher applied normal load caused the long hairs to buckle before sliding even started. This pre-sliding buckling is also the reason why the lateral force did not start from zero (marked with dotted circles in Fig. 5e) since the development of lateral forces started before the lateral displacement started. The initial friction could be either positive or negative, depending on the long hair buckling direction.

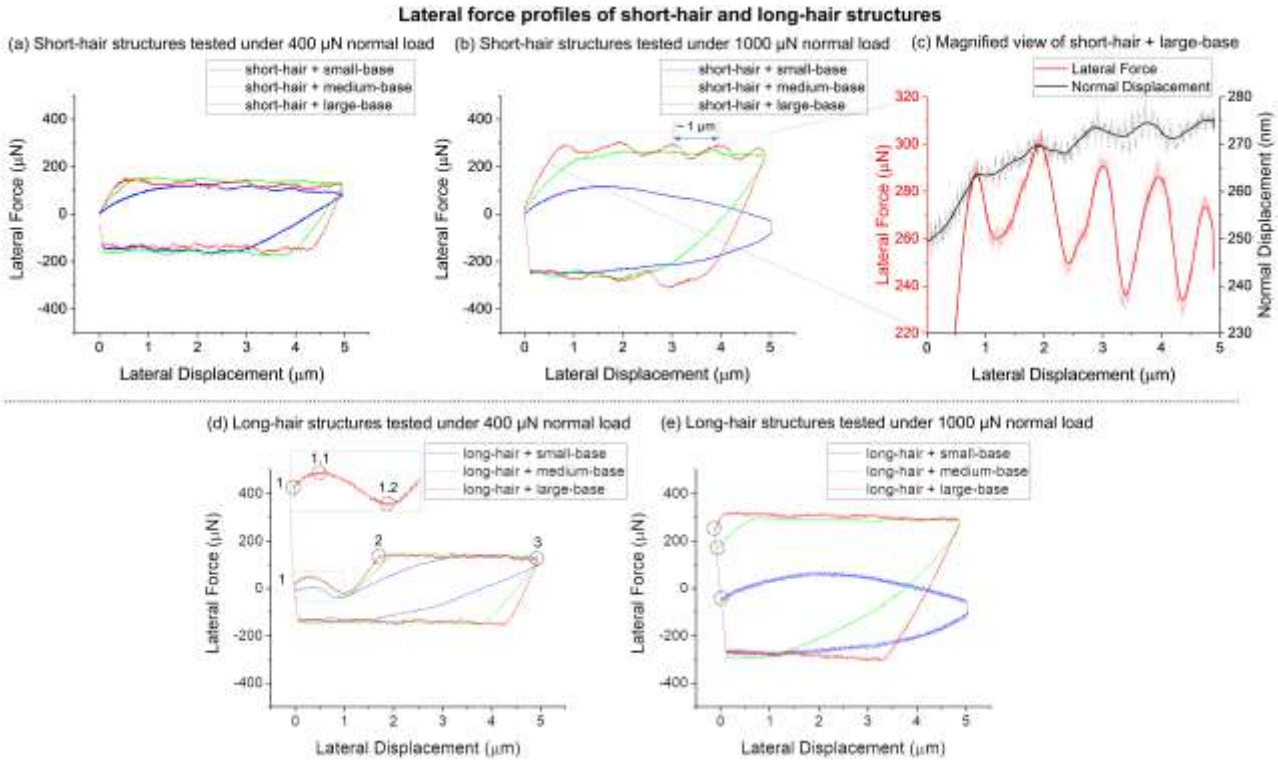

Fig. 5. Lateral force profiles for micro/nano-hierarchical structures: short-hair structures tested under (a) 400 μN and (b) 1000 μN applied normal load, (c) magnified view of the lateral force profile and normal displacement of the counterface during the forward stroke of the short-hair + large-base structure. Long-hair structures tested under (d) 400 μN and (e) 1000 μN applied normal load.

Another effect of increasing the length of the nanohair, besides making the nanohair itself less deformation-resistant, is how it results in changes in the deformation and friction mode (sliding vs. sticking) of the micropillar base. Fig. 6 shows the deformation of the small-base structures with different nanohair lengths captured as the forward stroke came to an end, accompanied by the lateral force profile when subjected to a normal load of 400 μN. The long-hair structure showed a significantly larger base deformation compared to the other two structure types. Here, the existence of long nanohairs on the small-base structure resulted in the sticking of

the contacting pair with no relative sliding, while for the short-hair and no-hair structures, relative sliding occurred. Video S2 in the Supplementary Material shows the sliding vs. sticking of different small-base structures shown in Fig. 6.

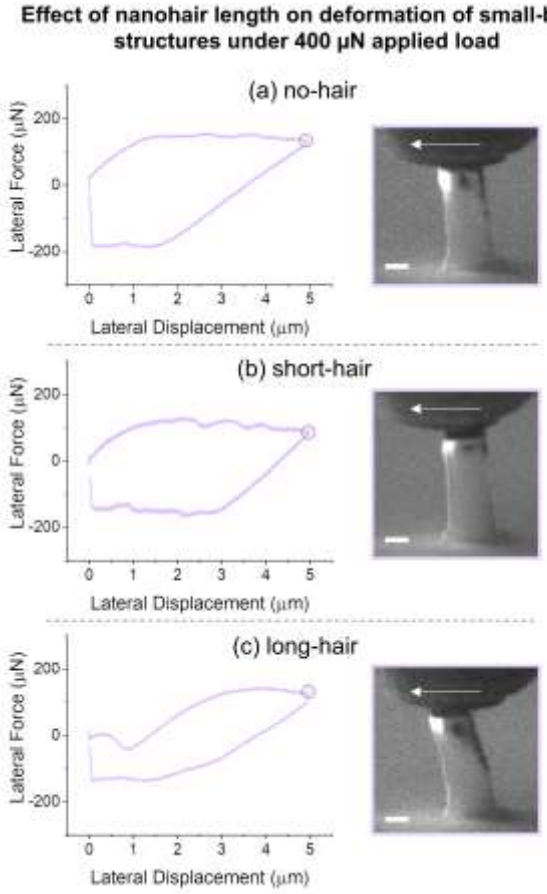

Fig. 6. Deformation of the small-base structures as a function of nanohair length for (a) no-hair, (b) short-hair, and (c) long-hair structures (scale bar: 2 μm).

3.5 Quantification of pre-sliding slopes

Fig. 7 shows the quantified values of the pre-sliding slopes as the lateral stiffnesses [50] of different structure types under various applied normal loads (400, 600, 800, and 1000 μN). It is evident that the micropillar base dimension, regardless of the nanohair height, was the dominant factor in determining lateral stiffness. The lateral stiffness increased as the micropillar base dimension increased. Long nanohairs reduced the lateral stiffness of all structures, and more so for structures with medium and large bases. Short nanohairs also reduced the lateral stiffness of the structures with the large base.

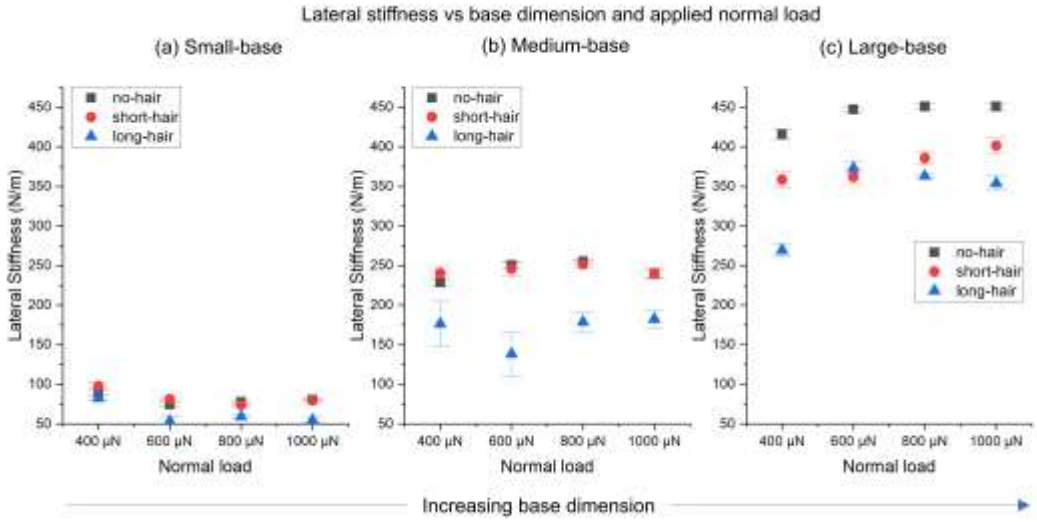

Fig. 7. Quantified values of pre-sliding slopes as the lateral stiffness of the structures for (a) small-base, (b) medium-base, and (c) large-base structures.

3.6 The effect of structural stiffness on the friction force

Fig. 8 presents the kinetic friction force (extracted from the lateral force profiles, such as in Figs. 3-5) of the micro/nano-hierarchical structures with different base dimensions and hair lengths when tested under different normal loads. For the small-base structures, the friction force under normal loads above 400 μN is not plotted since no relative motion occurred and there was no steady-state plateau in the lateral force profile. It is evident that, as the base dimension increased, the friction force and normal load had a more linear relationship. For all the structure types with medium and large bases, the no-hair structures have the greatest friction force under all applied normal loads, the short-hair structures have the smallest friction force, and the long-hair structures have a friction force between them. This is because the no-hair structures have the highest contact area, while the short hairs effectively reduced the area in contact. However, even though the long-hair structures have the same apparent contact area as the short-hair structures, the real contact area increased to be in between that of the short-hair and no-hair structures under normal load due to buckling-induced collapse of the long nanohairs.

In addition to the contact area, the stiffness of the structures also showed to affect the friction. As illustrated by the in-situ images in Fig. 4d-f, the increase in the stiffness of the structures (as the base dimension increased) reduced the bending of the structures. This resulted in a more linear relationship between the contact area and the applied normal load, and hence friction, as the base dimension increased. The 3D FEA simulation results shown in Fig. 8d-f are consistent with the experimental results. Since 3D models were only used for the FEA simulation of no-hair structures, only the FEA results of no-hair structures are shown in Fig. 8. FEA simulations of small-base structures showed steady-state friction under 600 μN normal load too, while

experiments showed steady-state friction under 400 μN normal load only. This difference could be due to the material calibration and Coulomb friction definition of the models.

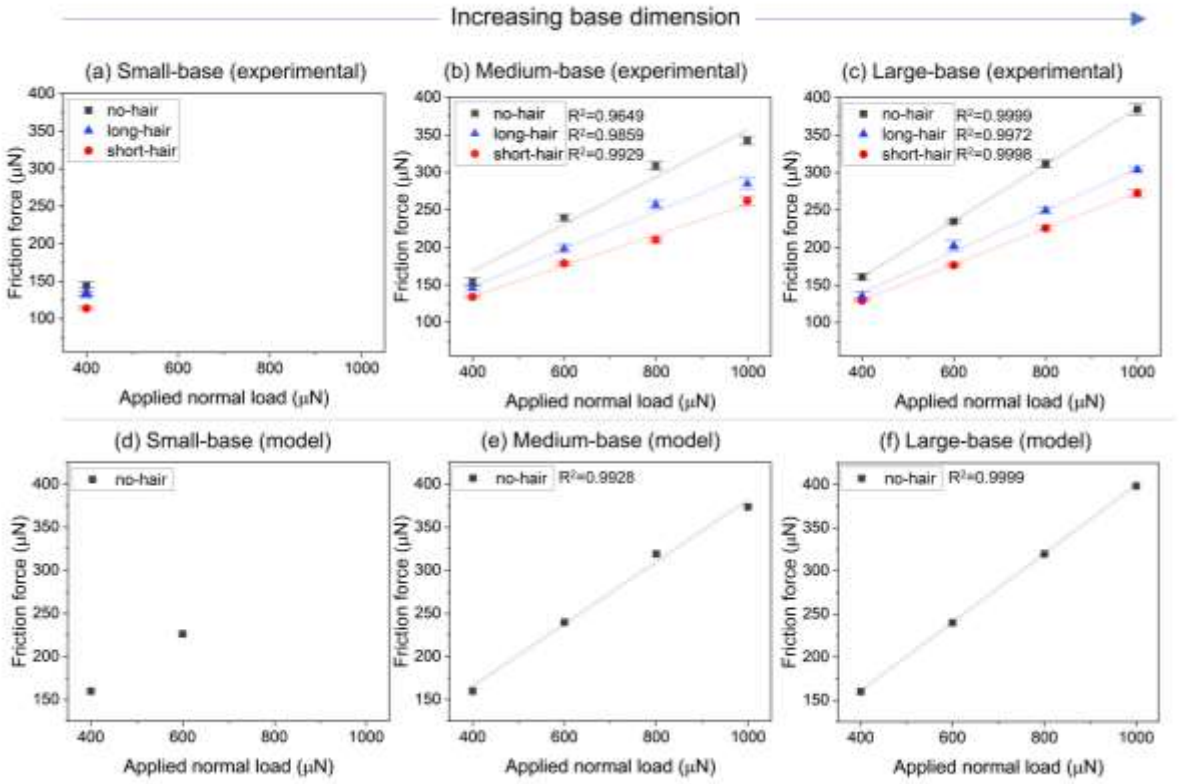

Fig. 8. Kinetic friction forces under various applied normal loads for structures with different structural stiffness. The friction force data for the small-base structure under a load above 400 μN (600 μN for modeling) is not plotted because no relative motion occurred.

3.7 Effect of micropillar base dimension on the critical buckling load of the long hairs

Fig. 9 shows the load-displacement curves of the tests during the initial loading, i.e., before sliding started (under the largest applied normal load of 1000 μN). There is a noticeable difference in the load-displacement curves for the long-hair structures (Fig. 9c), compared to no-hair (Fig. 9a) and short-hair (Fig. 9b) structures. Instead of normal displacement continually increasing with the applied normal load, there are points at which irregularities were initiated on the long-hair curves (outlined with the dashed circles in Fig. 9c), due to the buckling of the long nanohairs during the application of the normal load. It is evident from the curves in Fig. 9c that as the base dimensions of the micropillars increased, it took a larger normal load to cause buckling in the nanohairs. The dotted arrow in Fig. 9c shows the trend of the increasing critical buckling load as a result of increasing the base dimension of the micropillar underneath the long nanohairs.

The FEA results for long-hair structures (Fig. 9e) also confirm the relationship between the buckling of the long nanohairs and the base dimension of the micropillars. Although the values resulting from FEA tests are not the same as those from experiments, the same trend is observed whereby the larger base dimensions resulted in nanohair buckling at a higher applied normal load, as outlined using the dotted arrows and circles. Snapshots from the FEA model, together with the schematic view in Fig. 9d, show that as the long nanohairs go through different stages of buckling, they exert lateral force. Although only a normal load is applied, lateral forces start developing as a result of nanohair buckling, causing the bending of the micropillar underneath (FEM snapshot of point 2 in Fig. 9e). Bigger base dimensions provide more resistance to bending due to their higher moment of inertia/higher bending stiffness. The critical buckling force in a hierarchical structure hence corresponds to the normal force that induces enough lateral force to deform the

nanohairs to initiate the bending of the micropillar underneath (point 2 in Fig. 9e). Point 3 in Fig. 9e shows the complete collapse of the nanohairs.

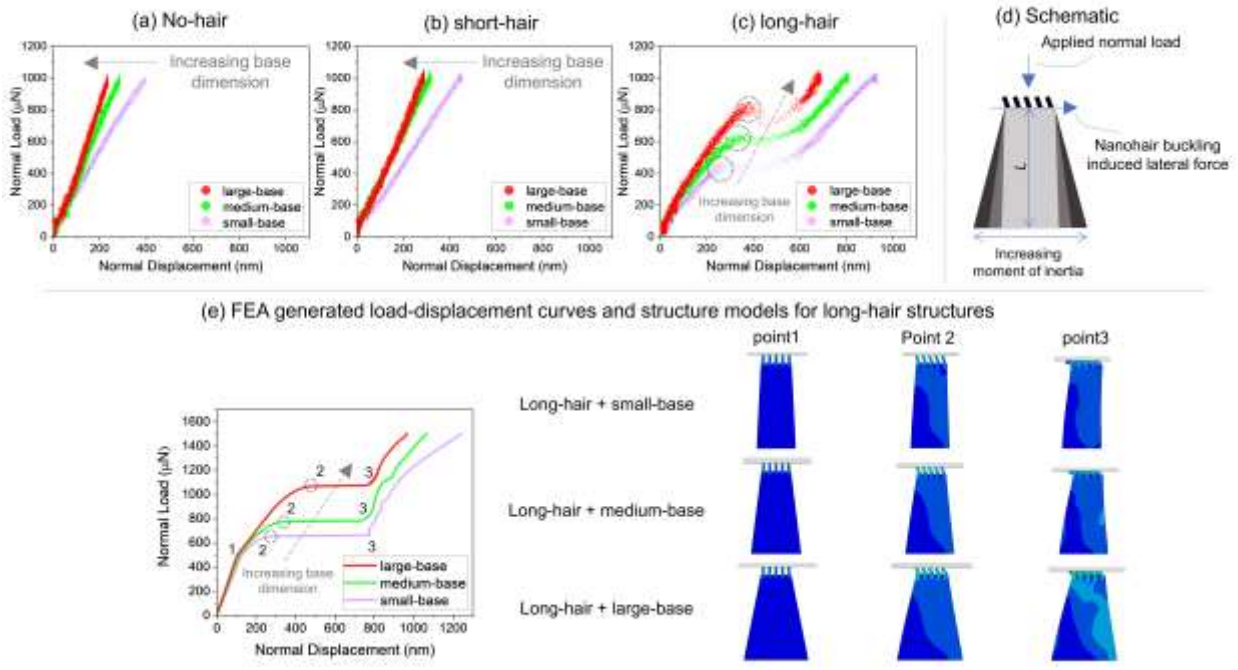

Fig. 9. Load-displacement curves extracted from the initial loading of the structures before the starting of lateral displacement for (a) no-hair, (b) short-hair, and (c) long-hair structures under the applied normal load of 1000 μN , (d) schematic of the buckling of the long nanohairs, and (e) FEA-generated load-displacement curves and structure models for long-hair structures.

It can be seen from Fig. 9 that in the pre-buckling region of the long-hair plots, the slope of the curves decreased as the applied normal load increased as opposed to the more constant slope of the no-hair and short-hair plots. This change in slope was relatively smooth and insignificant in the case of experimental results (Fig. 9c) while appearing as a more sudden change in the case of FEA results (Fig. 9e, point 1) as is evident by the sudden change around the applied normal load of 500 μN. The sudden change in the modeling results is due to the transition from elastic deformation to plastic deformation of the nanohairs. The contour plots of the equivalent plastic

strain in long-hair + medium-base structure shown in Fig. S1 Supplementary Material illustrate the elastic to plastic deformation transition.

3.8 Effect of 3D geometric variations on normal stiffness of structures

Although this study has mainly focused on the effects of structure shape on the friction force and lateral stiffness, we can also use the plots in Fig. 9 to examine the effect of the shape on the normal stiffness of the structures. Looking at the load-displacement curves of no-hair structures (Fig. 9a), it can be seen that the increasing base dimension resulted in a smaller normal displacement for the same applied normal load of 1000 μN as outlined using the dashed arrow. These curves were used to calculate the effective normal stiffness values presented in Fig. 10, which shows that the effective normal stiffness of the structures was reduced as a result of the addition of nanohairs and hence the existence of hierarchy. In the case of hierarchical structures, the increase in the length of the nanohairs also resulted in a reduction in the normal stiffness. The reduction in the effective stiffness with the addition of another level of hierarchy was also reported previously in similar micro/nano-hierarchical structures [44,45].

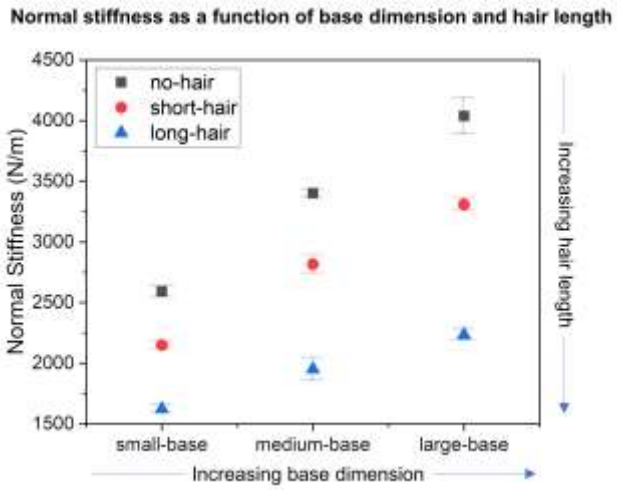

Fig. 10. Normal stiffness of the different structure types as a function of base dimension and hair length calculated from the load-displacement curves.

3.9 Hydrophobicity

Fig. 11 shows the measured WCA of textures (Fig. 11a), together with the summary of the results presented earlier, i.e., friction, normal stiffness, and lateral stiffness under the 1000 μN applied normal load (Figs. 11b-d). For WCA measurements, 3 × 3 mm surfaces made up of patterns of micro/nano-hierarchical structures were fabricated (shown in Fig. S2 Supplementary Material). Fig. 11 is an overview of the results in one place to facilitate their comparison which can offer general guidance in selecting the structure for a desired combination of properties. For example, a short-hair + large-base structure provides low friction as the short-hair texture reduced the contact area, while still maintaining a relatively high stiffness (small deformation) provided by its large base, and hydrophobicity (WCA of 144.1º ± 0.5º). Fig. S3 Supplementary Material provides more details regarding the WCA values.

Fig. 11a shows that increasing the base dimension of the micropillar did not considerably decrease the WCA, if at all. This means that the micropillar stiffness can be separately tuned by controlling the 3D shape to circumvent the inherent issue of reduced mechanical stability [32,51] when attempting to increase the WCA of surfaces using simple slender structures to trap air between the surface and water and reduce the contact area between them [52,53]. Long nanohairs were still required to transition from hydrophobic (~145º) to superhydrophobic (>150º), which lowered the effective stiffness. Despite this, the small-scale 3D shape control offered by TPL still

delivered improvements as the long nanohairs supported by a large-base micropillar were shown to have the advantage of having a higher critical buckling load than that supported by a small base or a medium base (section 3.7), delaying the nanohair failure.

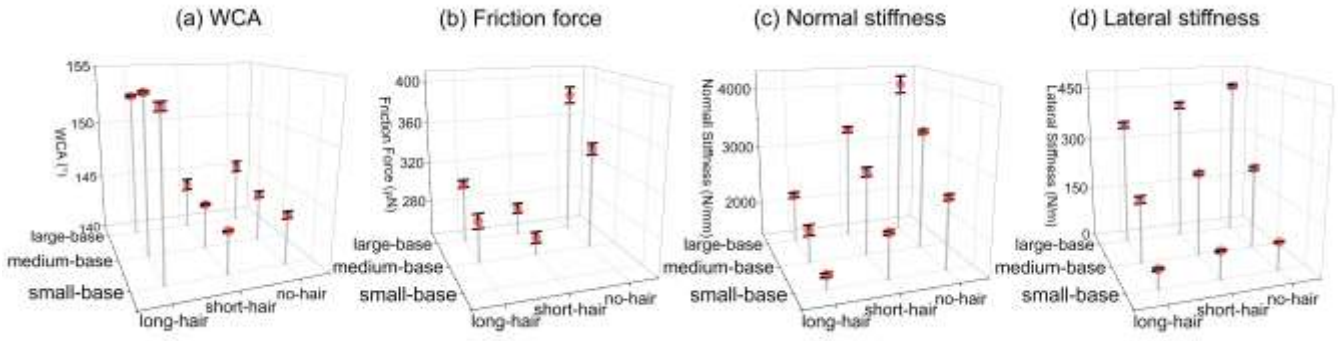

Fig. 11. Comparison of the effects of 3D shape control on (a) WCA, (b) friction force, (c) normal stiffness, and (d) lateral stiffness at 1000 μN normal load.

4. Conclusions

The versatility and resolution of TPL enabled control over the 3D shape and dimensions of fabricated micro/nano-hierarchical structures. Such control resulted in the ability to increase the stiffness and hence decrease the deformation of the structures. Additionally, the 3D variations in the shape of the structures showed to affect the onset of sliding motion, friction, friction-normal load relationship, WCA, and the interplay between the micro-nano scales structures.

Stiffer structures showed reduced lateral and normal deformation, earlier onset of relative sliding motion, and a more linear relationship between the friction force and the applied normal load. The addition of nanohairs reduced the effective stiffness and contact area of the structures.

Noteworthy interplays across the micro-nano scale structures were observed. The small-base micropillars with long nanohairs on top experienced complete bending under the smallest applied normal load while no-hair and short-hair structures did not, showing how the nanohair affected the behavior of the micropillar. Moreover, it was discovered that, as the micropillar base dimension increased, it took a larger applied normal load for the long nanohair to buckle. This, together with the fact that larger micropillar base dimensions did not reduce the WCA, provides a solution for addressing the inherent challenges of developing surfaces with high WCA with mechanical stability.

The combination of small-scale 3D printing (TPL), in-situ SEM monitoring of friction tests, and FEA modeling resulted in discoveries that can be used to guide the design of surfaces with desired properties. Using faster fabrication methods, such as shown in this study when replicating 3D printed structures and surfaces, can speed up the fabrication process while maintaining the accuracy, resolution, and versatility of 3D printing.

Acknowledgments

The research was supported by the U.S. National Science Foundation (NSF) under Grant no. CMS-1463306 and the Center for Advanced Surface Engineering under Grant no. OIA-1457888 and the Arkansas EPSCoR Program, ASSET III. The authors thank the Arkansas Biosciences Institute and the University of Arkansas for major equipment funding support. X.Y. and R.L. are supported by a CAREER award from the National Science Foundation (NSF CMMI-1752449).

References

[1] Z. Burton, B. Bhushan, Hydrophobicity, adhesion, and friction properties of nanopatterned polymers and scale dependence for micro- and nanoelectromechanical systems, Nano Lett. 5 (2005) 1607–1613. https://doi.org/10.1021/nl050861b.

[2] S.R. Maddox, A. Gangopadhyay, H. Ghaednia, J. Cai, X. Han, X. Meng, J.A. Goss, M. Zou, Fabrication and testing of bioinspired surface designs for friction reduction at the piston ring and liner interface, J. Tribol. 143 (2021). https://doi.org/10.1115/1.4050795.

[3] R.A. Fleming, M. Zou, Nanostructure-textured surfaces with low friction and high deformation resistance, Tribol. Trans. 61 (2018) 80–87. https://doi.org/10.1080/10402004.2016.1274066.

[4] A. Dunn, J. V. Carstensen, K.L. Wlodarczyk, E.B. Hansen, J. Gabzdyl, P.M. Harrison, J.D. Shephard, D.P. Hand, Nanosecond laser texturing for high friction applications, Opt. Lasers Eng. 62 (2014) 9–16. https://doi.org/10.1016/j.optlaseng.2014.05.003.

[5] J. Schille, F. Ullmann, L. Schneider, M. Graefensteiner, S. Schiefer, M. Gerlach, E. Leidich, H. Exner, Experimental study on laser surface texturing for friction coefficient enhancement, JLMN-Journal of Laser Micro/Nanoengineering. 10 (2015). https://doi.org/10.2961/jlmn.2015.03.0002.

[6] A. Dunn, K.L. Wlodarczyk, J. V. Carstensen, E.B. Hansen, J. Gabzdyl, P.M. Harrison, J.D. Shephard, D.P. Hand, Laser surface texturing for high friction contacts, Appl. Surf. Sci. 357 (2015) 2313–2319. https://doi.org/10.1016/J.APSUSC.2015.09.233.

[7] Y. Xing, J. Deng, Z. Wu, F. Wu, High friction and low wear properties of laser-textured ceramic surface under dry friction, Opt. Laser Technol. 93 (2017) 24–32. https://doi.org/10.1016/J.OPTLASTEC.2017.01.032.

[8] A. Samanta, W. Huang, M. Bell, S.K. Shaw, N. Charipar, H. Ding, Large-area surface wettability patterning of metal alloys via a maskless laser-assisted functionalization method, Appl. Surf. Sci. 568 (2021) 150788. https://doi.org/10.1016/J.APSUSC.2021.150788.

[9] Y. Sun, Z. Guo, Recent advances of bioinspired functional materials with specific wettability: from nature and beyond nature, Nanoscale Horizons. 4 (2018) 52–76. https://doi.org/10.1039/C8NH00223A.

[10] S.H. Anastasiadis, Development of functional polymer surfaces with controlled wettability, Langmuir. 29 (2013) 9277–9290. https://doi.org/10.1021/LA400533U.

[11] H. Shams, K. Basit, M.A. Khan, S. Saleem, A. Mansoor, Realizing surface amphiphobicity using 3D printing techniques: A critical move towards manufacturing low-cost reentrant geometries, Addit. Manuf. 38 (2021) 101777. https://doi.org/10.1016/J.ADDMA.2020.101777.

[12] Y. Liu, S. Li, S. Niu, X. Cao, Z. Han, L. Ren, Bio-inspired micro-nano structured surface with structural color and anisotropic wettability on Cu substrate, Appl. Surf. Sci. 379 (2016) 230–237. https://doi.org/10.1016/J.APSUSC.2016.03.234.

[13] Y. Wang, L. Shang, G. Chen, L. Sun, X. Zhang, Y. Zhao, Bioinspired structural color patch with anisotropic surface adhesion, Sci. Adv. 6 (2020). https://doi.org/10.1126/SCIADV.AAX8258.

[14] X. Zong, H. Bien, C.Y. Chung, L. Yin, D. Fang, B.S. Hsiao, B. Chu, E. Entcheva, Electrospun fine-textured scaffolds for heart tissue constructs, Biomaterials. 26 (2005) 5330–5338. https://doi.org/10.1016/J.BIOMATERIALS.2005.01.052.

[15] G. Hu, K. Guan, L. Lu, J. Zhang, N. Lu, Y. Guan, Engineered functional surfaces by laser microprocessing for biomedical applications, Engineering. 4 (2018) 822–830. https://doi.org/10.1016/J.ENG.2018.09.009.

[16] L. Chen, C. Yan, Z. Zheng, Functional polymer surfaces for controlling cell behaviors, Mater. Today. 21 (2018) 38–59. https://doi.org/10.1016/J.MATTOD.2017.07.002.

[17] E. Arzt, H. Quan, R.M. McMeeking, R. Hensel, Functional surface microstructures inspired by nature – From adhesion and wetting principles to sustainable new devices, Prog. Mater. Sci. 120 (2021) 100823. https://doi.org/10.1016/J.PMATSCI.2021.100823.

[18] W.-G. Bae, H.N. Kim, D. Kim, S.-H. Park, H.E. Jeong, K.-Y. Suh, 25th Anniversary Article: Scalable Multiscale Patterned Structures Inspired by Nature: the Role of Hierarchy, Adv. Mater. 26 (2014) 675–700. https://doi.org/10.1002/adma.201303412.

[19] K. Autumn, Y.A. Liang, S.T. Hsieh, W. Zesch, W.P. Chan, T.W. Kenny, R. Fearing, R.J. Full, Adhesive force of a single gecko foot-hair, Nature. 405 (2000) 681–685. http://dx.doi.org/10.1038/35015073.

[20] A.R. Parker, H.E. Townley, Biomimetics of photonic nanostructures, Nat. Nanotechnol. 2007 26. 2 (2007) 347–353. https://doi.org/10.1038/nnano.2007.152.

[21] L. Feng, Y. Zhang, J. Xi, Y. Zhu, N. Wang, F. Xia, L. Jiang, Petal effect: A superhydrophobic state with high adhesive force, Langmuir. 24 (2008) 4114–4119. https://doi.org/10.1021/LA703821H/SUPPL_FILE/LA703821H-FILE001.PDF.

[22] Y. Zheng, D. Han, J. Zhai, L. Jiang, In situ investigation on dynamic suspending of microdroplet on lotus leaf and gradient of wettable micro- and nanostructure from water condensation, Appl. Phys. Lett. 92 (2008) 084106. https://doi.org/10.1063/1.2887899.

[23] B. Bhushan, Y.C. Jung, Natural and biomimetic artificial surfaces for superhydrophobicity, self-cleaning, low adhesion, and drag reduction, Prog. Mater. Sci. 56 (2011) 1–108. https://doi.org/http://dx.doi.org/10.1016/j.pmatsci.2010.04.003.

[24] M. Elsharkawy, T.M. Schutzius, C.M. Megaridis, Inkjet patterned superhydrophobic paper for open-air surface microfluidic devices, Lab Chip. 14 (2014) 1168–1175. https://doi.org/10.1039/C3LC51248G.

[25] X. Gao, J. Zhou, R. Du, Z. Xie, S. Deng, R. Liu, Z. Liu, J. Zhang, Robust Superhydrophobic Foam: A Graphdiyne-Based Hierarchical Architecture for Oil/Water Separation, Adv. Mater. 28 (2016) 168–173. https://doi.org/10.1002/adma.201504407.

[26] Q. Pan, M. Wang, Miniature boats with striking loading capacity fabricated from

superhydrophobic copper meshes, ACS Appl. Mater. Interfaces. 1 (2009) 420–423. https://doi.org/10.1021/AM800116D/SUPPL_FILE/AM800116D_SI_001.PDF.

[27] H.S. Grewal, S. Piao, I.J. Cho, K.Y. Jhang, E.S. Yoon, Nanotribological and wetting performance of hierarchical patterns, Soft Matter. 12 (2016) 859–866. https://doi.org/10.1039/C5SM01649E.

[28] M. Zou, L. Cai, H. Wang, Adhesion and friction studies of a nano-textured surface produced by spin coating of colloidal silica nanoparticle solution, Tribol. Lett. 21 (2006) 25–30. https://doi.org/10.1007/s11249-005-9004-5.

[29] R.P. Nair, M. Zou, Surface-nano-texturing by aluminum-induced crystallization of amorphous silicon, Surf. Coatings Technol. 203 (2008) 675–679. https://doi.org/10.1016/j.surfcoat.2008.07.014.

[30] Y. Song, R. Premachandran Nair, M. Zou, Y.A. Wang, Adhesion and friction properties of micro/nano-engineered superhydrophobic/hydrophobic surfaces, Thin Solid Films. 518 (2010) 3801–3807. https://doi.org/doi.org/10.1016/j.tsf.2010.01.009.

[31] T. Verho, C. Bower, P. Andrew, S. Franssila, O. Ikkala, R.H.A. Ras, Mechanically durable superhydrophobic surfaces, Adv. Mater. 23 (2011) 673–678. https://doi.org/10.1002/adma.201003129.

[32] B.P. Dyett, A.H. Wu, R.N. Lamb, Mechanical stability of surface architecture—consequences for superhydrophobicity, ACS Appl. Mater. Interfaces. 6 (2014) 18380–18394. https://doi.org/10.1021/am505487r.

[33] Y. Kim, Y. Chung, A. Tsao, R. Maboudian, Tuning micropillar tapering for optimal friction performance of thermoplastic gecko-inspired adhesive, ACS Appl. Mater. Interfaces. 6 (2014) 6936–6943. https://doi.org/10.1021/AM5007518.

[34] Y. Cho, H.K. Minsky, Y. Jiang, K. Yin, K.T. Turner, S. Yang, Shear adhesion of tapered nanopillar arrays, ACS Appl. Mater. Interfaces. 10 (2018) 11391–11397. https://doi.org/10.1021/acsami.8b02303.

[35] D. Shin, D.G. Kang, K.Y. Woo, Y.-H. Cho, S.M. Han, D. Jang, Friction control by deformation mode in nanopatterned amorphous carbon, Nano Lett. 21 (2020) 107–113. https://doi.org/10.1021/ACS.NANOLETT.0C03339.

[36] K.B. Fritzler, V.Y. Prinz, 3D printing methods for micro- and nanostructures, Physics-Uspekhi. 62 (2019) 54–69. https://doi.org/10.3367/UFNE.2017.11.038239/XML.

[37] V.Y. Prinz, K.B. Fritzler, V.Y. Prinz, K.B. Fritzler, 3D Printed Biohybrid Microsystems, Adv. Mater. Technol. (2022) 2101633. https://doi.org/10.1002/ADMT.202101633.

[38] K. Muldoon, Y. Song, Z. Ahmad, X. Chen, M.W. Chang, High Precision 3D Printing for Micro to Nano Scale Biomedical and Electronic Devices, Micromachines 2022, Vol. 13, Page 642. 13 (2022) 642. https://doi.org/10.3390/MI13040642.

[39] T. Bückmann, N. Stenger, M. Kadic, J. Kaschke, A. Frölich, T. Kennerknecht, C. Eberl, M. Thiel, M. Wegener, Tailored 3D mechanical metamaterials made by dip-in direct-

laser-writing optical lithography, Adv. Mater. 24 (2012) 2710–2714. https://doi.org/10.1002/adma.201200584.

[40] M. Feinaeugle, R. Pohl, T. Bor, T. Vaneker, G. willem Römer, Printing of complex free-standing microstructures via laser-induced forward transfer (LIFT) of pure metal thin films, Addit. Manuf. 24 (2018) 391–399. https://doi.org/10.1016/J.ADDMA.2018.09.028.

[41] B.W. An, K. Kim, H. Lee, S.-Y. Kim, Y. Shim, D.-Y. Lee, J.Y. Song, J.-U. Park, B.W. An, K. Kim, H. Lee, S.-Y. Kim, Y. Shim, J.-U. Park, D.-Y. Lee, J.Y. Song, High-Resolution Printing of 3D Structures Using an Electrohydrodynamic Inkjet with Multiple Functional Inks, Adv. Mater. 27 (2015) 4322–4328. https://doi.org/10.1002/ADMA.201502092.

[42] M. Afshar-Mohajer, X. Yang, R. Long, M. Zou, Understanding the friction and deformation behavior of micro/nano-hierarchical textures through In-situ SEM observation and mechanics modeling, Tribol. Int. 165 (2021) 107271. https://doi.org/10.1016/j.triboint.2021.107271.

[43] N. Rohbeck, R. Ramachandramoorthy, D. Casari, P. Schürch, T.E.J. Edwards, L. Schilinsky, L. Philippe, J. Schwiedrzik, J. Michler, Effect of high strain rates and temperature on the micromechanical properties of 3D-printed polymer structures made by two-photon lithography, Mater. Des. 195 (2020) 108977. https://doi.org/https://doi.org/10.1016/j.matdes.2020.108977.

[44] C. Greiner, E. Arzt, A. del Campo, Hierarchical gecko-like adhesives, Adv. Mater. 21 (2009) 479–482. https://doi.org/10.1002/ADMA.200801548.

[45] H.K. Raut, A. Baji, H.H. Hariri, H. Parveen, G.S. Soh, H.Y. Low, K.L. Wood, Gecko-inspired dry adhesive based on micro–nanoscale hierarchical arrays for application in climbing devices, ACS Appl. Mater. Interfaces. 10 (2018) 1288–1296. https://doi.org/10.1021/acsami.7b09526.

[46] M. Afshar-Mohajer, M. Zou, Multi-Scale in situ tribological studies of surfaces with 3D textures fabricated via two-photon lithography and replica molding, Adv. Mater. Interfaces. 7 (2020) 2000299. https://doi.org/10.1002/admi.202000299.

[47] K. Suzuki, Y. Hirai, T. Ohzono, Oscillating friction on shape-tunable wrinkles, ACS Appl. Mater. Interfaces. 6 (2014) 10121–10131. https://doi.org/10.1021/am5010738.

[48] E. Wandersman, R. Candelier, G. Debrégeas, A. Prevost, Texture-induced modulations of friction force: The fingerprint effect, Phys. Rev. Lett. 107 (2011) 164301. https://doi.org/10.1103/PhysRevLett.107.164301.

[49] B. Khojasteh, M. Janko, Y. Visell, Complexity, rate, and scale in sliding friction dynamics between a finger and textured surface, Sci. Reports 2018 81. 8 (2018) 1–10. https://doi.org/10.1038/s41598-018-31818-3.

[50] R.W. Carpick, D.F. Ogletree, M. Salmeron, Lateral stiffness: A new nanomechanical measurement for the determination of shear strengths with friction force microscopy, Appl. Phys. Lett. 70 (1997) 1548–1550. https://doi.org/10.1063/1.118639.

[51] S. Sarbada, Y.C. Shin, Superhydrophobic contoured surfaces created on metal and polymer using a femtosecond laser, Appl. Surf. Sci. 405 (2017) 465–475. https://doi.org/10.1016/J.APSUSC.2017.02.019.

[52] Y. Yu, Z.-H. Zhao, Q.-S. Zheng, Mechanical and superhydrophobic stabilities of two-scale surfacial structure of lotus leaves, Langmuir. 23 (2007) 8212–8216. https://doi.org/10.1021/la7003485.

[53] K. Yamamoto, S. Ogata, 3-D thermodynamic analysis of superhydrophobic surfaces, J. Colloid Interface Sci. 326 (2008) 471–477. https://doi.org/10.1016/j.jcis.2008.06.044.

Supplementary Material

3D printing of micro/nano-hierarchical structures with various structural stiffness for controlling friction and deformation

Mahyar Afshar-Mohajer[1,2], Xingwei Yang[3], Rong Long[3], and Min Zou[1,2*]

[1]Department of Mechanical Engineering, University of Arkansas, Fayetteville, AR 72701, USA

[2]Center for Advanced Surface Engineering, University of Arkansas, Fayetteville, AR 72701, USA

[3]Department of Mechanical Engineering, University of Colorado Boulder, Boulder, CO 80309, USA

* Corresponding author, e-mail address: mzou@uark.edu.

Supplementary Figures

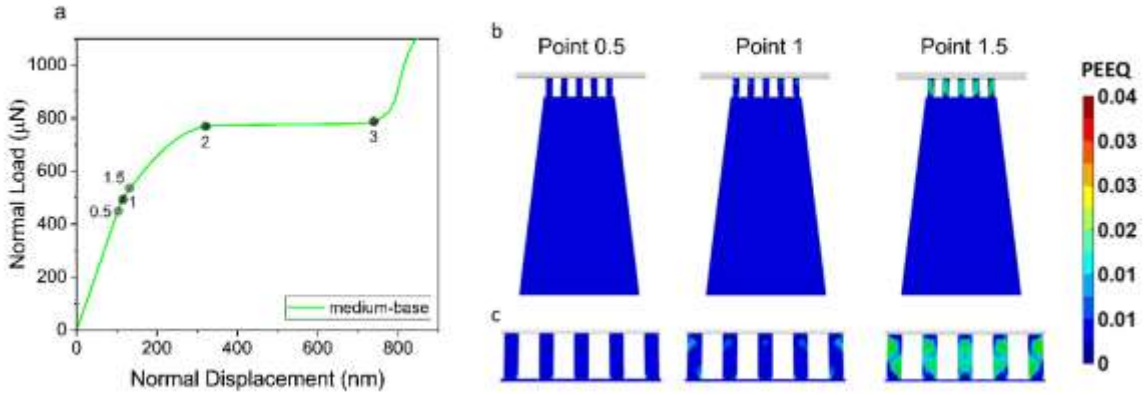

Fig. S1. Finite element analysis results of long-hair + medium-base structure. (a) Load-displacement result. (b) and (c) Equivalent plastic strain (PEEQ) contour plots for the (b) entire structure and (c) zoomed-in view of the nanohairs. The three points are around the slope transition region in the normal load versus normal displacement curve. The change of slope is due to the transition from elastic to plastic deformation.

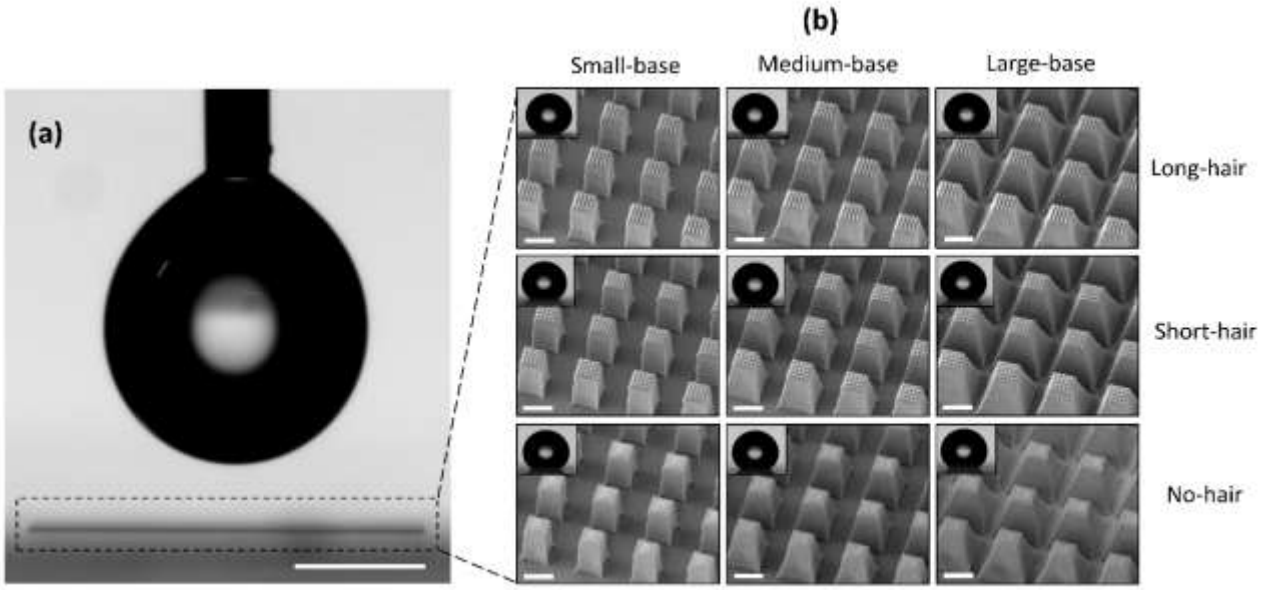

Fig. S2. (a) the larger area being tested for water contact angle (scale bar: 1 mm), and (b) the arrangement of the different structure types within the larger area (scale bars: 5 μm), the insets show the 9 μL water droplets deposited on each surface type.

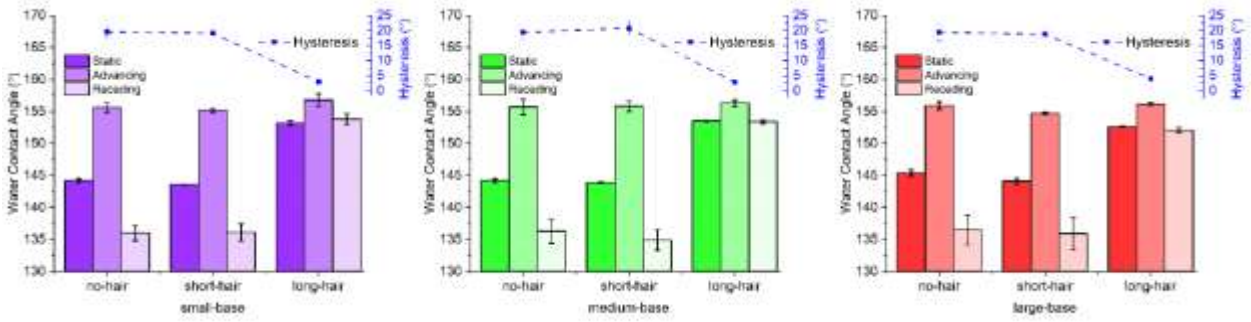

Fig. S3. Detailed WCA measurements of the surfaces including static, advancing, and receding WCAs and contact angle hysteresis.

Supplementary Videos

Video S1: In-situ SEM video (including the corresponding lateral force VS lateral displacement plot) of small-base structure with no-hair under 1000 μN normal load, showing no sliding between the counterface and the structure as the structure completely bends.

Video S2: In-situ SEM video (including the corresponding lateral force VS lateral displacement plot) of the small-base structures with no-hair, short-hair, and long-hair under 400 μN normal load, showing the sliding of no-hair and short-hair vs. sticking of long-hair structures.